PCCP

Accepted Manuscript

This article can be cited before page numbers have been issued, to do this please use: C. Penschke and J. Paier, *Phys. Chem. Chem. Phys.*, 2017, DOI: 10.1039/C7CP01785E.

ROYAL SOCIETY OF CHEMISTRY

rsc.li/pccp

View Article Online
DOI: 10.1039/C7CP01785E

Reduction and oxidation of Au adatoms on the CeO_2(111) surface – DFT+*U* versus hybrid functionals †

Christopher Penschke and Joachim Paier*

Recently we showed that Au atoms may titrate Ce^{3+} ions in near-surface layers of reduced CeO_2(111). This surface contained oxygen vacancies in subsurface position within the topmost O-Ce-O trilayer [Pan et al., *Phys. Rev. Lett.*, 2013, **111**, 206101.]. The present work builds upon these findings and discusses additional results obtained using PBE+*U* and hybrid functionals. These approaches do not predict the same relative stabilities for the various adsorption sites of a single Au adatom at an O-defect concentration of a $^1/_4$ ML or 1.984 nm^{-2}. We attribute this discrepancy to a different alignment within the O 2p–Ce 4f gap, i.e. a different order by energy of partially occupied Ce 4f and Au 6s orbitals. The energy offset of these orbitals matters, because the adsorption of $Au^0(6s^1)$ atop $Ce^{3+}(4f^1)$ or atop a subsurface oxygen atom in the first coordination shell of a $Ce^{3+}(4f^1)$ involves creation of $Au^-(6s^2)$ and $Ce^{4+}(4f^0)$ ions. The electron transfer to Au is coupled to stabilizing ionic relaxation in the lattice, commonly known as polaronic distortion, reinforcing the Au–Ce bond. The order of 4f and 6s orbitals depends on the density functional approximation and is also strongly influenced by the oxygen defect concentration.

Institut für Chemie, Humboldt-Universität zu Berlin, Unter den Linden 6, 10099 Berlin.
E-Mail: joachim.paier@chemie.hu-berlin.de

† Electronic supplementary information (ESI) available: Details of *GW* calculations, lattice parameters and bulk moduli of CeO_2, and total energies. See DOI:

View Article Online
DOI: 10.1039/C7CP01785E

1. Introduction

The pioneering work of Haruta on metal oxide supported Au nanoparticles revealed that these catalysts are highly active in many oxidation reactions[1-4] and drastically modified the view on noble metals in catalysis. Platinum or gold deposited on a reducible oxide support like ceria (CeO_2) form particularly active catalysts important in many technological processes, such as the water–gas shift reaction or low–temperature CO oxidation.[5-7] Atomistic insight is indispensable in order to understand the reasons for the observed catalytic activity, but disentangling individual relevant effects involved in a specific reaction is a formidable task. Especially metal–support interactions are complex, because many factors, such as binding site, size of metal clusters, support morphology (extended surface *versus* confined nanoparticle), and the distribution of charges may impact reactivity.[8-10]

Recently, Campbell emphasized the role of the so-called electronic metal–support interaction (EMSI), which conveys into strong chemical bonding between transition metal atoms and ceria.[11] EMSI involves electron transfer between metal ad-species and the ceria support, implying its partial reduction as indicated by the presence of Ce^{3+} ions.[12, 13] This effect occurs independently of the present ceria nanostructure. In contrast, morphology of the ceria support plays a decisive role in the interaction with surface oxygen atoms. For ceria nanoparticles oxygen spill-over from the support to the metal, necessitating formation of oxygen defects, is reported by Vayssilov et al.[13] However, this does not occur at perfectly ordered extended surfaces.

In addition to the metal ad-species, also oxygen defects may influence the charge or oxidation state of Ce^{4+} ions in ceria. Upon removal of an oxygen atom, the two remaining electrons easily occupy localized Ce 4f states creating two Ce^{3+} ions. Surface oxygen vacancies are important adsorption sites for noble metal atoms as found experimentally by Flytzani-Stephanopoulos and co-workers[6] as well as by Freund and co-workers.[14, 15] Additionally, surface O vacancies were identified as deep effective traps for Au atoms using

View Article Online
DOI: 10.1039/C7CP01785E

density functional theory (DFT). Depending on details of the approach, the adsorption energy of Au in the vacant site varies within -2.29 and -2.75 eV.[16-18]

From a theory point of view, the workhorse method for calculations on simple oxides is DFT employing conventional exchange-correlation (xc) functionals as, e.g., the local density (LDA) or generalized-gradient approximation (GGA). Despite their successes, these functionals are unable to correctly describe the aforementioned localized Ce 4f states due to self-interaction and related delocalization errors.[19-23] The DFT+*U* approach is commonly used to rectify this failure and to properly localize defect states. The method involves a Hubbard-type *U* term applied to the supposedly spatially confined, atom-like orbitals.[24, 25] The *U* parameter can be chosen such that calculated band gaps[26] or reaction energies[27, 28] agree with experiment, but also other methods exist to calculate *U* by virtue of first principles (see, e.g., refs. 29 and 30).

Hybrid functionals, which replace a certain fraction of the GGA exchange with orbital-dependent Fock exchange (FX), represent an alternative to DFT+*U* to at least partially rectify self-interaction errors.[31, 32] For hybrids, the increase in the computational workload compared to GGA may be substantial.[33-35] Nevertheless, Da Silva et al. conclude that hybrid functionals yield a more balanced description of the bulk properties of ceria compared with DFT+*U*.[21] Similar conclusions were drawn by Sanz and co-workers, who explored varying the amount of admixed FX in a hybrid functional when applied to ceria.[36] As shown in ref. 21, GGA+*U* based on the xc functional after Perdew, Burke, and Ernzerhof[37] (PBE) overestimates the equilibrium lattice constant and underestimates the reduction energy of CeO_2. A reasonable value of *U* acting on the Ce 4f orbitals (i.e. $U_{Ce\text{-}4f}$) is 4.5 eV and was calculated by Fabris and co-workers by virtue of linear response theory,[38] but other viable values ranging between 4 and 6 eV were explored by Hermansson and co-workers.[26] In contrast, hybrid functionals like HSE named after Heyd, Scuseria, and Ernzerhof,[39] predict values in excellent agreement with observation.[23, 40] However, similar to the DFT+*U* approach, whose results will depend on the

View Article Online
DOI: 10.1039/C7CP01785E

value of *U*, hybrid functional results will, e.g., depend on the amount of admixed FX. The abovementioned work by Sanz and coworkers showed that good agreement with experimental band gaps and reaction energies of cerium oxides is obtained with 8 – 16 % FX admixed in PBE0 calculations.[36]

A large body of theoretical work on the interaction of gold adatoms with the clean, fully oxidized CeO_2(111) surface has been published.[16, 17, 41-44] Zhang, Michaelides, and Jenkins recently reviewed results relying on GGA+*U* calculations.[45] They conclude that adsorption of Au at the O–O bridge site is the most stable configuration, while Au atop oxygen is about 200 meV less stable. Branda et al. examined the effect of the utilized density functional, the stability of Au on CeO_2(111) depending on its oxidation state, and the effect of strain by varying the unit cell parameter.[43] According to their results, the accurate prediction of the oxidation state of Au on CeO_2(111) appears to be difficult, since solutions for the minimum energy structure involving Au^0 or Au^+ atop a surface oxygen atom are *de facto* degenerate in energy using GGA+*U*. Furthermore, LDA+*U* predicts Au^+/CeO_2(111) to be lower in energy by 51 meV compared with Au^0 on the surface, but the HSE hybrid predicts Au^0/CeO_2(111) to be more stable by 150 meV. The latter finding is in agreement with recent STM results concluding on close-to-neutral charge states for Au atoms adsorbed on defect-poor ceria surfaces.[46]

The degree of complexity in the Au/ceria system increases significantly upon introduction of oxygen point defects. This is because the Au atom is not only exposed to Ce^{4+} and O^{2-}, but also to Ce^{3+} ions and the (electro-positively charged) vacancy. Concerning the position of the vacancy in the O^{2-} lattice of CeO_2(111), two possibilities are most relevant due to the stable O-Ce-O trilayer structure of the surface. The vacancy can either sit in the topmost layer (a surface vacancy) or in the next oxygen layer underneath the cerium layer (a subsurface vacancy). GGA+*U* results on the interaction of gold atoms with the surface vacancy are reported in refs. 47 and 17 as well as reviewed in ref. 45. Upon adsorption at the

View Article Online
DOI: 10.1039/C7CP01785E

vacant site, a 4f electron of a Ce^{3+} ion is transferred into the Au 6s orbital thereby creating a Ce^{4+} and a Au^{-}. This is a very exothermic process, because the negatively charged Au at the vacant site is electrostatically stabilized. Thus, it mimics an O^{2-} ion.[23]

In contrast, a direct interaction between Au atoms and a subsurface O vacancy is not possible. Instead, the defect-induced Ce^{3+} ions become potential adsorption sites. The interaction between Au atoms and Ce^{3+} ions associated with the subsurface O vacancy has been studied by STM and DFT recently.[48] The formation of subsurface O defects was controlled by the pressure of oxygen in the final annealing step. By virtue of low-temperature STM (ca. 10 K) characteristic Au pairs with Au–Au distances commensurate to the lattice of the CeO_2(111) surface were observed upon physical vapor deposition of Au. Importantly, the smallest pair distance found (~4.8 Å) is much larger than a typical Au–Au bond distance (~2.5 Å in the free molecule[49]). These Au pairs were found to be metastable species and could be rearranged to upright standing Au_2 dimers by applying a 3.0 V tip pulse. In several successful attempts, the subsurface vacancy in close vicinity to the Au pair could be identified experimentally.

These experiments have been combined with results obtained using the HSE hybrid functional. It was found that the 4f electron of a Ce^{3+} is transferred to Au, thus forming Au^{-}. The oxidation of Ce^{3+} induces structural relaxation, substantially lowering strain in the surface, which in turn reinforces the binding of Au on Ce^{3+}.

The present work examines the abovementioned Au/CeO_{2-x}(111) system more extensively using PBE+*U* as well as computationally more expensive, but supposedly more accurate, hybrid functionals like HSE and studies dependences on the *U* parameter and the amount of admixed FX. We emphasize that this work does not intend to offer the optimal set of parameters for employed methods reproducing observation. Instead, we intend to shed light on the physical principles underlying thermodynamic stabilities. Moreover, note that these

View Article Online
DOI: 10.1039/C7CP01785E

parameters (i.e., *U* as well as amount of FX) are motivated by quantum mechanics (see, e.g., ref. 40 and references therein). For instance, we discuss the relation between relative orbital energies (of electron donating and accepting orbitals) and thermodynamic stabilities of individual adsorption sites. Compared with HSE, PBE+*U* predicts that the relevant occupied Ce 4f electron donor level is substantially lower in energy than the half-filled Au 6s acceptor level. This renders the electron transfer from Ce^{3+} to the concomitantly reduced Au^0 unfavourable. In addition, the O-defect concentration affects 4f orbital energies, in turn impacting stabilities of adsorption sites. This demonstrates that the order by energy of electron donor and acceptor levels affects computed adsorption energies. Similar results for reduced TiO_2 were reported by Dupuis and coworkers.[50] In this work, we focus on thermodynamic stabilities of various electron distributions over adsorption sites, but the herein reported results are also relevant for kinetic electron transfer phenomena in reduced oxide surfaces.[51-54]

2. Computational details

A. Electronic and ionic structure optimizations

Calculations were performed using the projector augmented wave method (PAW)[55, 56] to describe the interaction between ionic cores and valence electrons as implemented in the Vienna *ab initio* simulation package (VASP).[57, 58] The PAW data sets released with VASP.5.2 were employed. Specifically, the "Au_pv_GW", "Ce_GW", and "O_GW" pseudopotentials, which include scalar relativistic corrections, were used. For Au, also the $5p^6$ electrons have been treated as valence electrons. Thus, Au uses 17 ($5p^6\ 5d^{10}\ 6s^1$), Ce uses 12 ($5s^2\ 5p^6\ 4f^1\ 5d^1\ 6s^2$), and O uses 6 ($2s^2\ 2p^4$) valence electrons in total. Spin-polarized calculations use a plane-wave cutoff of 600 eV and a Gaussian smearing of 0.02 eV width.

View Article Online
DOI: 10.1039/C7CP01785E

With regard to DFT+*U* calculations, we use both the LDA as well as the gradient-corrected PBE[32] xc functionals. Unless stated otherwise, LDA and PBE calculations use an *effective* $U_{\text{Ce-4f}}$ parameter of 5.3 and 4.5 eV (see ref. 38), respectively. The specific implementation of DFT+*U* used in this work follows Dudarev *et al*.[59, 60] Forces in DFT+*U* structure optimizations were converged to better than 0.02 eV/Å employing a break criterion for the electronic optimization of 10^{-6} eV.

With regard to hybrid functional calculations, results reported in this work use the HSE (HSE06),[61] PBE0,[62, 63] B3LYP, [31, 86, 87] and TPSSh[64] functionals. TPSSh mixes 10% FX and 90% of the meta-GGA TPSS exchange[65] as implemented in VASP.[66] The hybrid version of TPSS is based on a local modification of VASP. Test calculations on atomization energies of small molecules to check for correctness of the implementation are given in the ESI.† Since this work studies charge or electron localization in context of self-interaction errors in semilocal xc functionals, additional calculations with 50% of FX were accomplished based on HSE, PBE0, and B3LYP. With this amount of FX, B3LYP is equivalent to the so-called "Half-and-Half" functional after Becke, i.e. BHLYP.[67] The screening parameter in HSE for the range-separation was not varied (i.e., HSE06 with 0.207 $Å^{-1}$ [61]). All hybrid calculations, except those using TPSSh, employ surface unit cells with consistent lattice parameters (see ESI†). TPSSh calculations are single-points on top of HSE structures. Note that TPSSh and HSE lattice parameters as well as bulk moduli are similar. Regarding ionic relaxations using hybrids, the plane wave cutoff determining the Fourier grid for the FX related routines was equal to the plane wave cutoff applied to expand the orbitals (PRECFOCK = normal). Atomic forces have been converged to better than 0.04 eV/Å using an SCF break criterion of 10^{-5} eV.

The effect of van der Waals-type dispersion interactions was estimated for selected structures using the approach after Grimme.[68] Adsorption energies employing the correction for dispersion effects are more exothermic by 0.10 to 0.28 eV (see Table S6 in the ESI†).

View Article Online
DOI: 10.1039/C7CP01785E

However, relative stabilities of structures are not affected. Thus, we report uncorrected results in the present work.

We checked by normal mode analysis whether structures obtained with PBE+*U* correspond to true (local) minima. Calculations used central differences to compute the gradient of forces for the Hessian or force constant matrix. The applied step size in the atomic Cartesian coordinates is 0.02 Å. In structures employing a $p(2 \times 2)$ $CeO_2(111)$ surface unit cell (see section 2.C), all atoms (including Au) of the first CeO_2 trilayer are free to move when calculating force constants, while calculations using a $p(4 \times 4)$ cell include a sufficient number of atoms centred around the Au adsorbate (typically three to five atoms).

B. Orbitally projected densities of states

Projected densities of states (PDOS) and local magnetic moments of Ce and Au atoms are obtained by projection of crystal orbitals into spherical harmonics of f or s symmetry located in atom-centred PAW spheres with respective radii of 1.323 and 1.376 Å. A typical value for the local magnetic moment of $Ce^{3+}(4f^1)$ is $\pm 0.96\ \mu_B$ for up and down spins, respectively. For $Au^0(6s^1)$ atoms, the total moment is $\sim 0.4\ \mu_B$. Note that it involves 6s as well as 5d contributions. Magnetic moments of Ce and Au atoms for the various functionals are given in the ESI†. As expected, hybrid functionals using 50% FX show a more pronounced tendency to localize electrons compared with results obtained using 25%. Therefore, corresponding values of local magnetic moments are slightly larger than those obtained with hybrids employing less FX. TPSSh single-point calculations at HSE structures lead to a partial delocalization of the O-defect related electrons. To test whether these electrons localize upon ionic relaxation, we optimized the Au atop Ce^{3+} structure in $p(2 \times 2)$ $CeO_{2-x}(111)$. Upon reaching convergence, the so-called excess electrons delocalized completely over three Ce ions leading to a local magnetic moment of $\sim 0.3\ \mu_B$ per ion. Similarly, delocalization occurred upon optimizing atomic positions in the Au atop O_{surf} structure (see below). To double-check

View Article Online
DOI: 10.1039/C7CP01785E

this behavior, we repeated the calculations using HSE with 10% FX starting from properly converged HSE (25% FX) orbitals having the excess electrons correctly localized. HSE (10% FX) also predicts delocalized defect-related electrons resulting in a distribution of magnetic moments over Ce ions like in TPSSh results. Hence, TPSSh does not properly describe O-defect related electrons in CeO_{2-x}(111) surfaces. Single-point calculations employing TPSSh with 20% FX restore the proper localization of electrons and spins.

View Article Online
DOI: 10.1039/C7CP01785E

C. Surface models

The surface models were built by cutting the bulk cell using optimized lattice parameters corresponding to respective functionals along the [111] plane. Lattice constants and bulk moduli of CeO_2 for the various DFT approaches were obtained by fitting single point total energies for different cell volumes to Murnaghan's equation of state[69] (seven points within steps of ±1% centred around the equilibrium lattice constant). These results are presented in the ESI†. Slab models use nine atomic layers (i.e. three trilayers), resulting in a composition of $Ce_{12}O_{24}$ and $Ce_{48}O_{96}$ for $p(2 \times 2)$ and $p(4 \times 4)$ cells, respectively. We use asymmetric slab models, i.e. atomic positions in the lowest CeO_2 trilayer were fixed. The Brillouin zone was sampled with a Γ-centered $2 \times 2 \times 1$ Monkhorst-Pack[70] mesh for the $p(2 \times 2)$ cell, while the Γ point was used to sample the Brillouin zone of the $p(4 \times 4)$ cell. Test calculations showed that the applied vacuum layer of 10 Å suffices to avoid interactions between replicated images. Dipole and quadrupole interactions between consecutive surfaces are negligibly small as tested by applying the method after Makov and Payne.[71] Note that the electron transfer reactions studied in the present work refer to "local" electron transfer between different sites in the slab models used. Thus, slabs used in the present work maintain electro-neutrality.

3. Results and discussion

A. Comparison of LDA+*U*, PBE+*U*, and HSE for $p(2 \times 2)$ cells

Prior to Au adsorption, the most stable structure for $CeO_{2-x}(111)$ with a subsurface O defect using the $p(2 \times 2)$ cell is characterized by one Ce^{3+} located in the surface cation layer, whereas the second one is located in the subsurface cation layer.[72] Au adsorption energies and relative stabilities obtained using LDA+*U*, PBE+*U*, and HSE for adsorption atop Ce^{3+} (Fig. 1a), O_{sub} (Fig. 1b) and O_{surf} (Fig. 1c), as well as at the oxygen-oxygen bridge site (Fig. 1d), are compiled in Table 1. Additionally, adsorption of a Au atom at (i) the hollow site

View Article Online
DOI: 10.1039/C7CP01785E

on top of the subsurface vacancy (referred to as atop V_{sub} throughout the present work) and (ii) the Ce^{4+} ion was also studied. Importantly, the difference between Ce^{3+} atop and Ce^{4+} atop structures is in the origin of the transferred electron, which stems from the subsurface and surface cation layer, respectively. The more stable Ce^{3+} atop structure was mentioned in a note added in proof of ref. 48. Furthermore, the O_{surf} atop structure discussed in the present work involves a slightly larger tilting of the Au-O bond with respect to the surface normal (ca. 20.2°; see Fig. 1e).

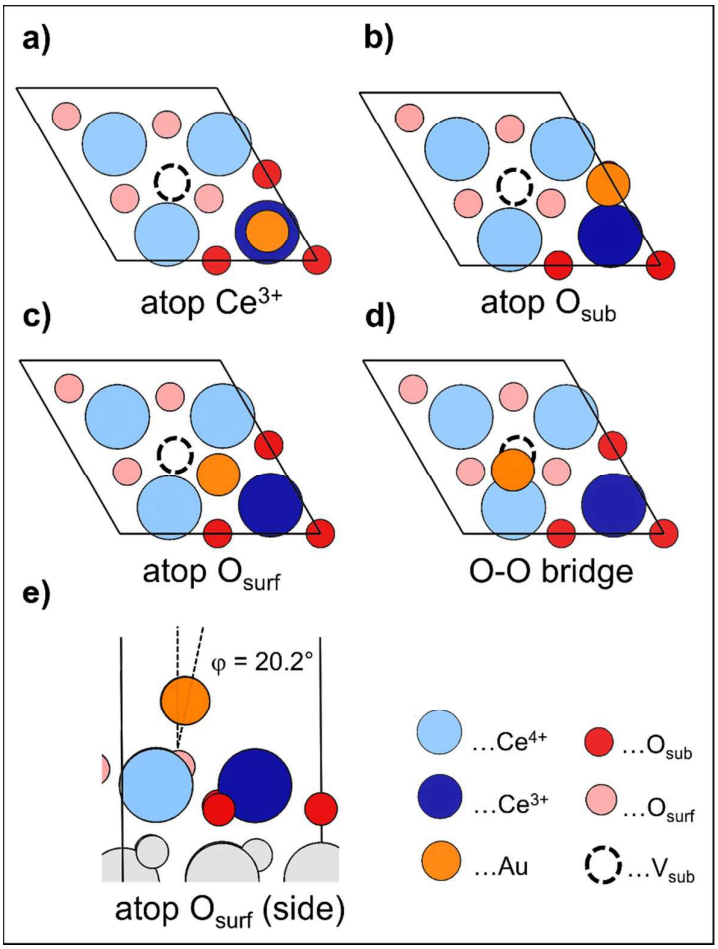

Fig. 1 Adsorption sites of a single Au atom on reduced CeO_2(111) containing a subsurface O vacancy [*p*(2 x 2) unit cell; atop a Ce^{3+} a); atop a subsurface O[73] b); atop a surface O c); O-O bridge site d)]. e) shows the tilting of the Au-O bond in structure c).

View Article Online
DOI: 10.1039/C7CP01785E

LDA+*U*, PBE+*U* and HSE predict the O_{sub} atop position to be the most stable adsorption site, while relative stabilities for the remaining adsorption sites depend on the employed density functional approximation (DFA). In terms of stability, O_{sub} atop is followed by Au in atop position of V_{sub} using LDA+*U*, while PBE+*U* and HSE predict V_{sub} atop to be least stable. Relative energies for Au atop Ce^{3+}, Ce^{4+}, and O_{surf} are almost identical using LDA+*U*. No minimum could be found for Au at the O–O bridge site using the LDA+*U* approach. Several attempts to locate the corresponding minimum energy structure led on to an Au atom adsorbed atop V_{sub} at the end of the optimization.

Table 1 Adsorption energy (eV) of a single Au atom on reduced CeO_2(111) containing a subsurface O vacancy [*p*(2 x 2) unit cell]. Relative energies are given in parentheses.

Adsorption site	LDA+*U*		PBE+*U*		HSE	
O_{sub} atop	-1.85	(0)	-0.95	(0)	-0.95	(0)
Ce^{3+} atop	-1.30	(+0.55)	-0.64	(+0.30)	-0.64	(+0.31)
Ce^{4+} atop	-1.29	(+0.56)	-0.61	(+0.34)	-0.58	(+0.38)
O_{surf} atop	-1.28	(+0.57)	-0.78	(+0.16)	-0.55	(+0.40)
O-O bridge	[a]	(–[a])	-0.69	(+0.25)	-0.24	(+0.71)
V_{sub} atop	-1.63	(+0.22)	-0.55	(+0.40)	+0.09	(+1.05)

[a] Not stable; Au converges into the V_{sub} atop position (see text).

Table 2 Bond distances (Å) of a single Au atom on reduced CeO_2(111) containing a subsurface O vacancy [*p*(2 x 2) unit cell]. Au-O tilting angles w.r.t. the surface normal are given in parentheses. For bidentate (O-O bridge) and tridentate (O_{sub} atop, $V_{O\text{-}sub}$ atop) Au, average values are reported (see text).

Adsorption site	LDA+*U*	PBE+*U*	HSE
O_{sub} atop	2.997 (O)	3.144 (O)	3.140 (O)
	3.111 (Ce)	3.249 (Ce)	3.244 (Ce)
Ce^{3+} atop	2.793	2.882	2.894
Ce^{4+} atop	2.717	2.809	2.805
O_{surf} atop	2.118 (10.5)	2.209 (23.2)	2.212 (20.2)
O-O bridge	–[a]	2.196 (O)	2.790 (O)
		2.874 (Ce)	3.193 (Ce)
V_{sub} atop	2.222 (O)	2.301 (O)	2.322 (O)
	2.938 (Ce)	3.089 (Ce)	3.103 (Ce)

[a] Not stable; Au converges into the V_{sub} atop position (see text).

View Article Online
DOI: 10.1039/C7CP01785E

Table 3 Oxidation state (OS) of Au and the Ce^{3+} configuration within the cell for various adsorption structures in the *p*(2 x 2) cell of CeO_2(111) containing a subsurface O vacancy.

adsorption site	LDA+*U*		PBE+*U*		HSE	
	OS(Au)	Ce^{3+}	OS(Au)	Ce^{3+}	OS(Au)	Ce^{3+}
O_{sub} atop	-1	2_1[a]	-1	2_1	-1	2_1
Ce^{3+} atop	-1	2_1	-1	2_1	-1	2_1
Ce^{4+} atop	-1	2_2	-1	2_2	-1	2_2
O_{surf} atop	0	2_1-2_2	0	2_1-2_2	0	2_1-2_2
O-O bridge	[b]	[b]	+1	1_1-2_1-2_2	0	2_1-2_2
V_{sub} atop	+1	1_1-2_1-2_2	+1	1_1-2_2-2_2	+1	1_1-2_1-2_2

[a] The notation n_m refers to the n^{th} coordination shell of Ce ions around the vacancy and the m^{th} Ce-ion layer in the slab and applies to each Ce^{3+} in the cell.[74]
[b] Not stable; Au converges into the V_{sub} atop position (see text).

PBE+*U* predicts that Au atop O_{surf} is more stable by 0.14 eV compared to Au atop Ce^{3+} (see Table 1). In contrast, HSE predicts that Au atop Ce^{3+} is more stable by 0.09 eV compared to Au atop O_{surf}. As discussed above, adsorption of Au atop Ce^{3+} and atop Ce^{4+} involves electron transfer from the subsurface and surface cation layer, respectively. Oxidation of the subsurface Ce^{3+} ion to Ce^{4+} (and concomitant reduction of Au^0 to Au^-) is energetically more favourable by 0.03 eV (0.06 eV) compared to oxidation of the surface Ce^{3+} ion using PBE+*U* (HSE). In other words, Au^- adsorbed in atop position of Ce^{3+} is more stable than atop Ce^{4+} using a $p(2 \times 2)$ cell corresponding to an O-defect concentration of ¼ ML (≡ 1.984 nm^{-2}). Using PBE+*U*, a third solution involving partial electron transfer, i.e. $Au^{\delta-}$ associated with two partially reduced Ce ions, is 0.01 eV less stable than Au^- atop Ce^{3+}.

To check for the driving force on the oxidation of Ce^{3+} in surface and subsurface positions excluding relaxation effects induced by the formation of an oxygen vacancy, we put a Na adatom in a larger $p(4 \times 4)$ pristine CeO_2(111) unit cell. After optimization, a Na^+ ion and a Ce^{3+} ion are formed. We succeeded in creating a structure with a Na^+–Ce^{3+} distance of more than 6 Å. Thus, we believe the Ce^{3+} site to be unaffected from the Na dopant. The Ce^{3+} ion in

View Article Online
DOI: 10.1039/C7CP01785E

the second cation layer (i.e. Ce^{3+} in subsurface position) is less stable than the Ce^{3+} in the surface layer (see section 6 in the ESI†). These calculations use LDA+*U*, PBE+*U*, and HSE and consistently confirm this trend. The energy difference is, depending on the approach, 0.10 to 0.38 eV. Analysing the corresponding PDOS, this is consistent with a $4f^1$ orbital energy corresponding to the *subsurface* Ce^{3+} that is 0.40 (0.10) eV higher than the $4f^1$ energy of the *surface* Ce^{3+} measured relative to the O 2p valence band edge using HSE (PBE+*U*).

Table 2 presents relevant bond distances and tilting angles of the aforementioned adsorption structures. LDA+*U* predicts bond distances to be approximately 0.1 Å shorter compared to PBE+*U* and HSE results. For Au adsorbed on top of oxygen, a tilting of the Au atom towards the V_{sub} atop site was found. In contrast, Au is tilted towards the surface Ce^{3+} cation using PBE+*U* and HSE. Hence, this structure may also be considered as a Au atom adsorbed at the O-Ce bridge site. Bond distances obtained with HSE compare well with PBE+*U* results, except for the O–O bridge adsorption structure featuring a Au–O distance which is 0.6 Å longer than the corresponding PBE+*U* result. This is plausible, because the hybrid functional does not predict charge or electron transfer from Au to the surface (see Table 3), whereas PBE+*U* favours formation of Au^+, which attractively interacts with the two oxygen anions reinforcing the bond.

Table 3 summarizes oxidation states of the Au adatom depending on the adsorption site for various DFA approximations. Au in atop position of Ce^{3+} always adopts oxidation state (OS) −1. Thus, an electron was transferred from the surface to the Au adatom independent of the DFA. We reiterate that the electron transfer may follow two routes. Either the 4f electron of the Ce^{3+} directly underneath the Au adatom or alternatively the electron of the Ce^{3+} in subsurface position may be transferred into the Au 6s orbital. In contrast, Au remains electro-neutral or adopts oxidation state +1 at the various O sites. We emphasize that PBE+*U* and HSE disagree on the OS for Au at the O–O bridge site.

View Article Online
DOI: 10.1039/C7CP01785E

B. Electronic structure details of $p(2 \times 2)$ cells

Figure 2 compares the orbitally projected densities of states (PDOS) calculated using LDA+*U*, PBE+*U*, and HSE for Au adsorbed in atop position of O_{surf} and Ce^{3+} sites. These two sites were chosen because their relative stabilities depend on the DFA employed.

HSE (see Fig. 2c) predicts a larger gap between occupied O 2p and unoccupied Ce 4f states. Regarding the adsorption at O_{surf}, the occupied Au 6s state is ca. 1 eV lower in energy than the highest occupied 4f orbital being a Ce^{3+}-related defect state. Projecting layer-by-layer, one realizes that the highest occupied 4f orbital corresponds to the subsurface Ce^{3+} ion (see also section 3.A). The second Ce^{3+}-related 4f state is close in energy compared with Au 6s and splits into two peaks most likely due to a crystal-field effect induced by the Au atom. LDA+*U* and PBE+*U* predict subsurface Ce 4f and Au 6s to be *de facto* energetically degenerate. The energy gap between surface and subsurface Ce^{3+} $4f^1$ states is larger compared to the $p(4 \times 4)$ cell with a Na adatom (see section 3.A). LDA+*U*, PBE+*U*, as well as HSE predict the $4f^1$ orbital in subsurface position to be 0.5-0.6 eV higher in energy than the $4f^1$ stemming from a surface Ce^{3+}.

The PDOS for Au atop Ce^{3+} indicates the formation of a Au^- anion with a symmetric up and down spin component of the Au 6s orbital. The integrals of the spin-resolved peaks are equal, indicating occupation of one electron per spin channel, i.e. formation of Au^- with a doubly occupied $6s^2$ orbital. Using HSE, the PDOS of Au 6s (spin down) is hidden by the PDOS of the 4f orbital corresponding to the surface Ce^{3+}, which may indicate that the two atoms interact. This appears plausible, because the atoms are spatially close to each other enabling overlap between the 6s and 4f orbitals, and these orbitals are also close in energy. The Au 5d orbitals are substantially higher in energy than the O 2p band. This contrasts with the PDOS of Au atop O_{surf} featuring Au 5d states within the O 2p valence band.

View Article Online
DOI: 10.1039/C7CP01785E

The characteristics of the PDOS (lhs and rhs of Fig. 2c) are qualitatively reflected in relative stabilities shown in Table 1. Considering Au atop O_{surf}, essentially two effects may contribute when the Au adatom is transferred to Ce^{3+}: (i) energy gain upon transfer of the highest occupied $4f^1$ electron (subsurface Ce^{3+}) into Au 6s and (ii) destabilizing upshift of Au $5d^{10}$, $6s^2$, and Ce $4f^1$ orbitals w.r.t. the valence band edge. Effect (i) solely based on orbital energy differences suggests an energy gain of ca. 0.8 eV. This amount of energy certainly overestimates the energy difference between Au atop Ce^{3+} and Au atop O_{surf} structures. As shown in Table 1, HSE predicts 0.09 eV, a value almost one order of magnitude smaller. A large contribution to this decrease in relative stability is due to effect (ii). Figure 2b (lhs) shows that Au $6s^1$ and Ce $4f^1$ orbital energies coincide using PBE+*U*, implying negligible stabilization by (i). Therefore, effect (ii) dominates and consequently Au atop Ce^{3+} is less stable than Au atop O_{surf}. In contrast, these two adsorption sites are *de facto* degenerate in energy using LDA+*U* although a very similar PDOS is obtained (see Fig. 2a). This points out the limits of interpreting DFT orbital energies as so-called quasi-particle energies representing particle excitations.[75]

View Article Online
DOI: 10.1039/C7CP01785E

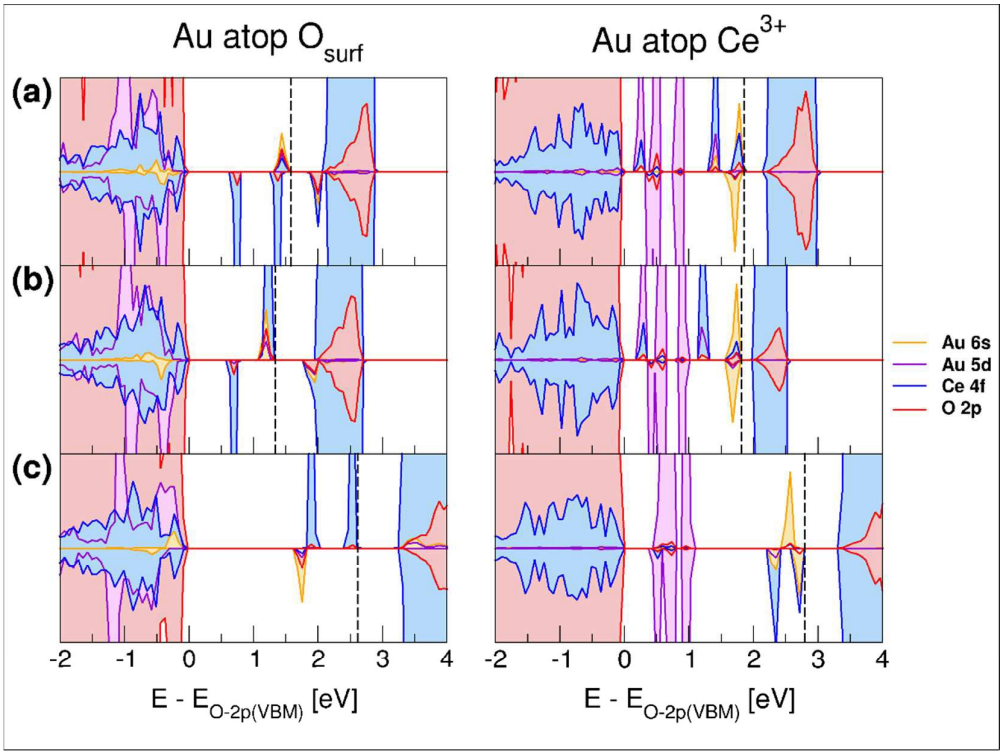

Fig. 2 Orbitally projected densities of states (PDOS) for Au adsorbed atop O_{surf} (left) and atop Ce^{3+} (right) using LDA+*U* (a), PBE+*U* (b) and HSE (c). Upper and lower half of each panel shows the up- and down-spin PDOS, respectively, aligned to the O 2p valence band maximum (VBM). The dashed line indicates the highest occupied energy level.

View Article Online
DOI: 10.1039/C7CP01785E

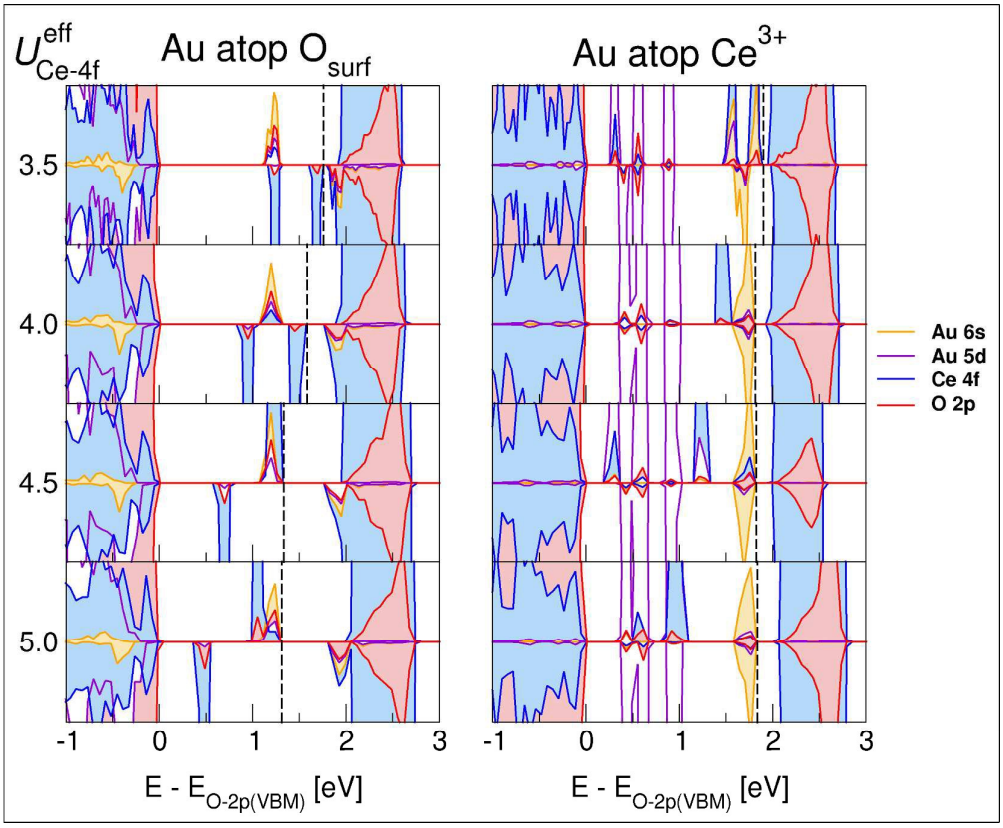

Fig. 3 PDOS of Au adsorbed atop O_{surf} (left) and atop Ce^{3+} (right) on the reduced CeO_2(111) surface using PBE+*U* with $U_{Ce\text{-}4f}$ = 3.5, 4.0, 4.5, and 5.0 eV, aligned to the O 2p valence band maximum (VBM). The dashed line indicates the highest occupied energy level.

C. Effects upon varying U_{eff}

Upon increasing $U_{Ce\text{-}4f}$ in PBE+*U* calculations, the occupied 4f states are, as expected, shifted towards lower energies (see Fig. 3). For Au adsorbed in atop position of O_{surf}, the effect is readily seen. The energy offset of the 4f orbital related to subsurface Ce^{3+} relative to the Au 6s state is strongly influenced. This 4f level is higher in energy for $U_{Ce\text{-}4f} = 4$ eV, is energetically degenerate for $U_{Ce\text{-}4f} = 4.5$ eV, and is lower in energy than the Au 6s orbital for $U_{Ce\text{-}4f} = 5$ eV.

To analyse the influence of the $U_{Ce\text{-}4f}$ parameter on adsorption energies, we varied $U_{Ce\text{-}4f}$ within a range of 3.5 and 5 eV in steps of 0.5 eV. The relative stability of the O_{surf} site compared to the Ce^{3+} site behaves proportional to the $U_{Ce\text{-}4f}$ parameter. The Ce^{3+} site is more

View Article Online
DOI: 10.1039/C7CP01785E

stable by 0.09 eV than Au atop O_{surf} using $U_{Ce\text{-}4f} = 3.5$ eV, while it is 0.21 eV higher in energy for $U_{Ce\text{-}4f} = 5$ eV.

The interaction between Au and Ce was also studied by applying respective U parameters to Au 6s ($U_{Au\text{-}6s}$) and 5d ($U_{Au\text{-}5d}$) states. We varied $U_{Au\text{-}6s}$ between 0.5 and 3 eV in steps of 0.5 eV, while keeping $U_{Ce\text{-}4f}$ constant at 4.5 eV. Increasing $U_{Au\text{-}6s}$ results in rather uniformly increasing total energies for both adsorption sites. Therefore, relative stabilities remained invariant with $U_{Au\text{-}6s}$ (see Fig. 4). Additional calculations with a $U_{Au\text{-}6s}$ of 4, 5 and 6 eV confirmed that this holds true for even larger values of $U_{Au\text{-}6s}$.

The oxidation state of Au in atop position of Ce^{3+} depends on $U_{Au\text{-}6s}$. Complete charge transfer, creating a Au^- anion, is energetically favoured for $U_{Au\text{-}6s}$ values up to 1.5 eV, partial charge transfer from the surface leading to $Au^{\delta-}$ is more favourable for $U_{Au\text{-}6s} \geq 2.0$ eV. The energy difference between these two charge states may be as large as 0.27 eV (partially charged Au more stable). The Au–Ce bond distance is ca. 0.1 to 0.2 Å larger in case of partial charge transfer compared with Au^- atop Ce^{3+}.

For Au atop O_{surf}, the Au adatom remains electro-neutral in the ground state. However, for some of the applied $U_{Au\text{-}6s}$ values an additional solution involving partially oxidized $Au^{\delta+}$ was also found. Independent of $U_{Au\text{-}6s}$, the partially positively charged Au adsorbed at the surface is ~0.13 eV less stable compared with Au^0. Regarding Au^0 atop O, the Au–O bond is tilted by ca. 20° relative to the surface normal, while $Au^{\delta+}$ sits in perfect atop position (i.e., no tilting).

View Article Online
DOI: 10.1039/C7CP01785E

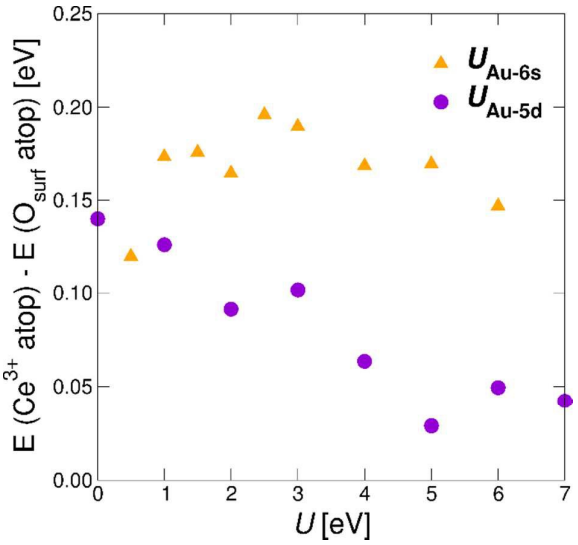

Fig. 4 Energy difference between Au atop Ce^{3+} and Au atop O_{surf} in the $p(2 \times 2)$ cell of $CeO_2(111)$ with one subsurface O vacancy as a function of $U_{Au\text{-}6s}$ (gold) and $U_{Au\text{-}5d}$ (violet).

The $U_{Au\text{-}5d}$ value was varied between 1 and 7 eV in steps of 1 eV, keeping $U_{Ce\text{-}4f}$ constant at 4.5 eV. Increasing $U_{Au\text{-}5d}$ leads to a nonlinear increase of the total energy. However, the energy increase behaves in a site-specific manner, i.e. the energy of Au atop O_{surf} approaches the energy of Au atop Ce^{3+} upon increasing the $U_{Au\text{-}5d}$ (see Fig. 4). Thus, at large $U_{Au\text{-}5d}$ values, both adsorption sites are *de facto* equally favourable, with a difference in relative energies of only 0.03 eV using a $U_{Au\text{-}5d} = 5$ eV.

The oxidation state of Au in atop position of Ce^{3+} depends on the $U_{Au\text{-}5d}$ value. Conventional PBE+$U_{Ce\text{-}4f}$(4.5) or utilization of an additional (small) $U_{Au\text{-}5d}$ value of 1 eV results in a complete electron transfer creating a Au^- anion, while electron delocalization or partial charge transfer involving a $Au^{\delta-}$ is energetically preferred for $U_{Au\text{-}5d} \geq 2$ eV. Upon increasing $U_{Au\text{-}5d}$, the energy difference between complete and partial charge transfer increases up to a maximum value of 0.2 eV for $U_{Au\text{-}5d} = 6$ eV. For $U_{Au\text{-}5d} = 7$ eV, only partial charge transfer was found. Similar to the scenario described for $U_{Au\text{-}6s}$, both Au^0 as well as $Au^{\delta+}$ solutions

View Article Online
DOI: 10.1039/C7CP01785E

exist, but for Au atop O the electro-neutral Au^0 is more stable for all of the $U_{Au\text{-}5d}$ values tested in the present work.

Based on the above mentioned findings, an interaction between Au 6s and 5d orbitals is obvious. This is due to relativistic effects and has been amply discussed by Pyykkö.[49] Moreover, from a methodological point of view, a *consistent* treatment of Au 6s and 5d orbitals appears mandatory. This requirement is naturally met by hybrid functionals, but appears to be difficult to fulfil within the DFT+*U* approach.

D. Performance of other hybrid functionals for *p*(2 × 2) cells

HSE, PBE0, and B3LYP predict the same qualitative picture in terms of electronic structure (PDOS). The PDOS obtained using HSE (see Fig. 5) is representative for corresponding results obtained with PBE0 or B3LYP (see ESI†). Increasing the amount of FX in HSE to 50% shifts the occupied Ce $4f^1$ orbitals (of both, surface and subsurface Ce^{3+}) substantially below the Au 6s state. Analogous results are obtained for PBE0 (50% FX) and BHLYP.

In terms of electron localization, TPSSh results differ from those obtained using HSE, PBE0, or B3LYP. For Au adsorbed on Ce^{3+}, TPSSh predicts partial delocalization of the 4f electron into subsurface Ce 4f orbitals. Consequently, the former surface Ce^{3+} ion carries a smaller local magnetic moment of 0.76 μ_B compared to 0.96 μ_B (see section 2.B). Similar delocalization of 4f electrons occurs in O_{surf} and O_{sub} atop structures. It appears that 10% of FX admixed in TPSSh is not sufficient to localize Ce 4f electrons. A test using HSE with 10% FX also leads to delocalization of these 4f electrons.

View Article Online
DOI: 10.1039/C7CP01785E

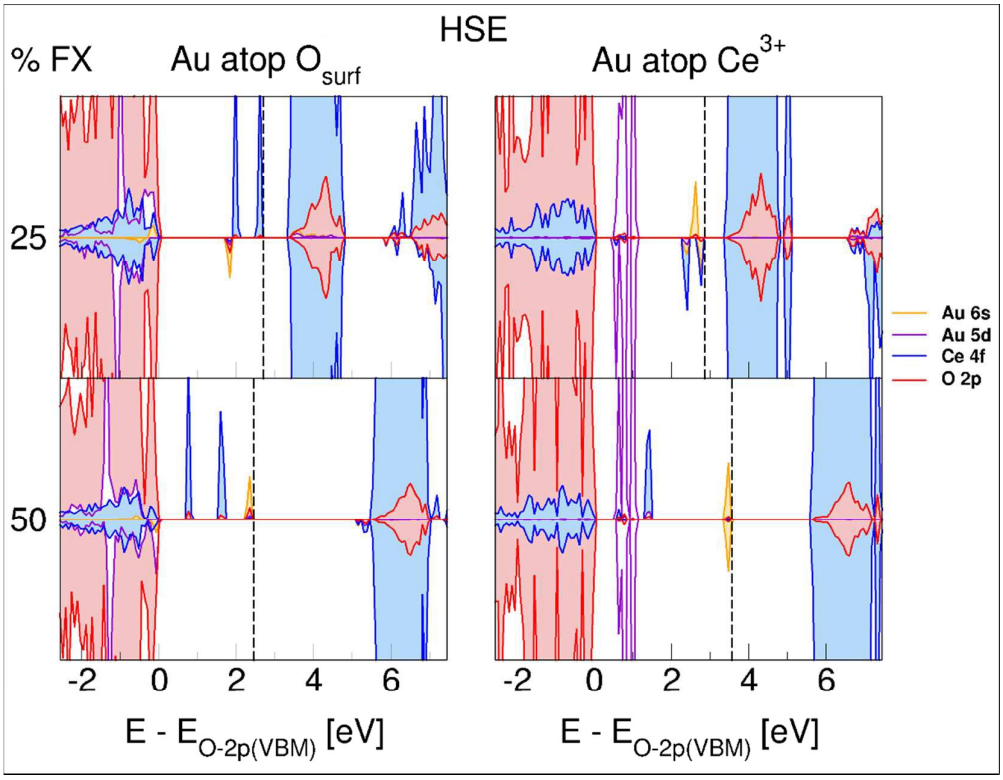

Fig. 5 PDOS of Au adsorbed atop O_{surf} (left) and atop Ce^{3+} (right) on the reduced CeO_2(111) surface, using HSE with 25% (top) and 50% (bottom) FX, aligned to the O 2p valence band maximum (VBM). The dashed line indicates the highest occupied energy level.

Relative energies and adsorption energies (see Tables 4 and 5) critically depend on the functional. HSE, PBE0, and TPSSh using the "as defined" amount of FX predict the O_{sub} atop position to be the most stable adsorption site for a single Au atom. However, B3LYP slightly favours the atop position of Ce^{3+}. Depending on the employed functional, the O_{surf} atop site is less stable than the Ce^{3+} atop site by 0.08 to 0.38 eV.

Increasing the amount of FX to 50% using HSE, PBE0 and B3LYP (= BHLYP) changes the relative stability in favour of the O_{surf} site. It is more stable by 0.42 to 0.59 eV relative to the Ce^{3+} atop site (see Tables 4 and 5). Thus, in analogy to PBE+*U* results discussed in section 3.C, we infer a correlation between relative stabilities of electron donor (Ce 4f) and acceptor (Au 6s) levels and the atop Ce^{3+} and atop O_{surf} sites. While adsorbing Au atop Ce^{3+} involves electron transfer or equivalently reduction of Au, adsorption in atop position of O_{surf} does not.

View Article Online
DOI: 10.1039/C7CP01785E

In the latter case, the 4f orbitals remain partially occupied and hence contribute to the relative stability. Conversely, the energy difference between Au atop Ce^{3+} and Au atop O_{sub} is largely unaffected by the amount of FX because in both structures a Au^- anion is formed leading to a consistent cancellation of energy contributions.

Validity of the alignment of Ce 4f and Au 6s orbitals relative to the O 2p valence band maximum was tested using non-selfconsistent as well as partially selfconsistent *GW* calculations (see Figure S3 in the ESI†). These rather computationally expensive calculations have been accomplished for Au in atop position of Ce^{3+} using the $p(2 \times 2)$ unit cell. According to results discussed in ref. 76, HSE orbitals and orbital energies have been used as an input. While HSE predicts virtually degenerate Ce $4f^1$ and Au $6s^2$ orbitals, *GW* results indicate a pronounced stabilization of the Au $6s^2$ orbitals. Also, the Au $5d^{10}$ orbitals, which are rather high in energy referenced to the O 2p valence band edge, move back into the valence band employing non-selfconsistent and selfconsistent *GW* and are thus stabilized. The *GW* results, as the supposedly more accurate reference, suggest that electron transfer from Ce^{3+} ($4f^1$) to Au^0 ($6s^1$) is even more favourable than predicted by HSE. In consequence, the Au atop Ce^{3+} structure is expected to be further stabilized relative to Au atop O_{surf} utilizing more accurate methods.

Table 4 Relative energies in eV for various adsorption sites in the *p*(2 x 2) cell of CeO_2(111) with one subsurface O vacancy.

DFA	a_{FX}	O_{surf} atop	Ce^{3+} atop	O_{sub} atop
HSE	0.25	+0.40	+0.31	**0.00**
	0.50	**0.00**	+0.42	+0.13
B3LYP	0.20	+0.08	**0.00**	+0.07
BHLYP	0.50	**0.00**	+0.59	+0.62
PBE0	0.25	+0.38	+0.29	**0.00**
	0.50	**0.00**	+0.45	+0.19
TPSSh	0.10	+0.74	+0.36	**0.00**

Table 5 Adsorption energies in eV for various adsorption sites in the *p*(2 x 2) cell of CeO_2(111) with one subsurface O vacancy.

View Article Online
DOI: 10.1039/C7CP01785E

DFA	a_{FX}	O_{surf} atop	Ce^{3+} atop	O_{sub} atop
HSE	0.25	-0.55	-0.64	**-0.95**
	0.50	**-0.42**	+0.01	-0.29
B3LYP	0.20	-0.44	**-0.52**	-0.45
BHLYP	0.50	**-0.22**	+0.37	+0.41
PBE0	0.25	-0.52	-0.62	**-0.91**
	0.50	**-0.32**	+0.13	-0.13
TPSSh	0.10	-0.57	-0.95	**-1.31**

E. Significance of the defect concentration

Table 6 Adsorption energies (eV/atom) for one Au atom and the vertical Au_2 dimer on the pristine $CeO_2(111)$ surface.

DFA	site	*OS*(Au)	$p(2 \times 2)$	*OS*(Au)	$p(4 \times 4)$
PBE+*U*	O-O bridge	+1	-1.20	+1	-1.35
	O_{surf} atop	+1	-1.07	+1	-1.24
	O_{sub} atop	+1	-1.05[a]	+1	-1.11[a]
		0	-0.61[b]	–	–
	O-Ce bridge[c]	0	-0.79[a]	+1	-1.01
	Ce^{4+} atop	0	-0.40[b]	0	-0.58[b]
	Au_2 atop O_{surf}	0	-1.83	0	-1.85
HSE	O_{surf} atop	0	-0.48	0	-0.52
	O-Ce bridge[c]	0	-0.52	0	-0.53
	O-O bridge	+1	-0.43	+1	-0.53
		0	-0.31	0	-0.30
	Au_2 atop O_{surf}	0	-1.58	0	-1.63

[a] One imaginary frequency.
[b] Two imaginary frequencies.
[c] Tilting angle of the Au-O bond w.r.t. surface normal ~27°.

Table 6 shows PBE+*U* and HSE adsorption energies of a single Au atom and the vertical Au_2 dimer on the pristine $CeO_2(111)$ surface using both $p(2 \times 2)$ and $p(4 \times 4)$ unit cells. Independent of cell size, the Au_2 dimer is the most stable adsorption structure regardless of the DFA. Employing PBE+*U*, the O-O bridge site is the most stable adsorption site involving

View Article Online
DOI: 10.1039/C7CP01785E

a single Au atom in oxidation state (OS) +1, which agrees with results reported in ref. 45. When Au adsorbs in atop position of a surface oxygen atom, it accommodates the oxidation state +1 and the structure is 0.13 eV less stable compared with the O-O bridge site. Note that relative stabilities do not change significantly using the $p(4 \times 4)$ cell, however, the adsorption proceeds substantially more exothermically, which is due to the lower Ce^{3+} concentration (less strain). Although technical convergence for the structure optimization was reached, the other adsorption structures, i.e. O_{sub} atop, O-Ce bridge, and Ce^{4+} atop, were identified as saddle points on the PBE+*U* potential energy surface using the $p(2 \times 2)$ cell. The O-Ce bridge site using a $p(4 \times 4)$ cell, however, is a local minimum as confirmed by normal mode analysis. For the structures found using PBE+*U*, analogous HSE calculations have been accomplished. Using the $p(2 \times 2)$ cell, Au^0 at the O-Ce bridge site is the most stable adsorption structure. It is 0.05 eV more stable than Au^0 atop O_{surf}. These two adsorption sites are structurally similar. The main difference is a larger tilting angle of the Au-O bond for Au in O-Ce bridge position, while Au-O bond distances hardly deviate. A Au^+ in atop position of O_{surf} was not considered in the present work, but as reported in ref. 43, it is about 0.15 eV higher in energy. For the adsorption of Au on the O-O bridge site, we found both solutions involving Au^0 and Au^+, the latter being 0.11 eV more stable. Au^+ in O-O bridge position is 0.10 eV less stable than Au^0 in O-Ce bridge position. These relative stabilities agree with the results reported by Branda et al. using GGA+*U* with $U_{Ce\text{-}4f}$ = 3 eV and a lattice constant of 5.40 Å (i.e., close to the experimental value).[43] In the $p(4 \times 4)$ cell, Au^0 at the O-Ce bridge site, Au^0 atop O_{surf} and Au^+ in O-O bridge position are *de facto* degenerate in energy.

In contrast to HSE, PBE+*U* adsorption energies are more exothermic and the PBE+*U* method favours Au^+ over Au^0. This can be readily explained by the position of Ce 4f orbitals in the gap, which is affected by $U_{Ce\text{-}4f}$ (see section 3.C.).[77, 78] The lower the energy of the Ce 4f orbitals, the more favourable their occupation. In addition, Ce^{3+} formation–as occurring upon oxidation of Au^0 to Au^+–induces strain in the surface due to the larger ionic radius of Ce^{3+}

View Article Online
DOI: 10.1039/C7CP01785E

compared with Ce^{4+}. This elastic contribution to the total energy depends on two factors: (i) the description by the DFA approximation of elastic properties such as the bulk modulus of the material and (ii) the size of the surface unit cell. The smaller the cell, the higher the Ce^{3+} concentration, which in turn relates to more pronounced and hence more stabilizing relaxation effects upon oxidizing Ce^{3+}.

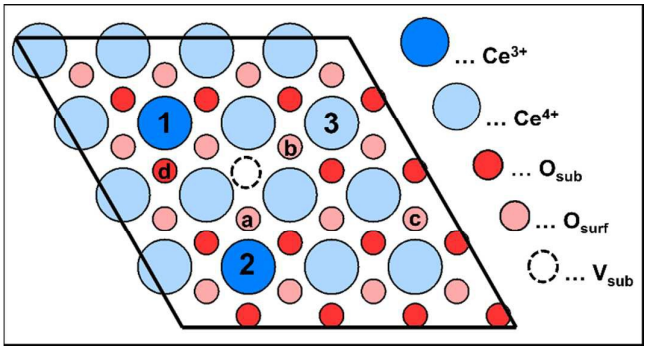

Fig. 6 Adsorption sites of a single Au atom on reduced $CeO_2(111)$ containing one subsurface O vacancy in the $p(4 \times 4)$ surface unit cell. The two Ce^{3+} ions in the structure prior to Au adsorption (i.e. the ground state, see ref. [48]) are marked by **1** and **2**. The site marked by **3** indicates the electron accepting Ce^{4+}, when Au adsorbs at the site bridging O_{surf} **a** and **b** (PBE+*U*, see text). O_{surf} close to V_{sub} and a Ce^{3+} ion is marked by **a**, O_{surf} close to V_{sub} is marked by **b**, O_{surf} far from V_{sub} (and Ce^{3+}) is marked by **c**. The O_{sub} site close to Ce^{3+}, as discussed in ref. [73], is marked by **d**.

Figure 6 shows the $p(4 \times 4)$ unit cell of $CeO_2(111)$ with one subsurface oxygen vacancy prior to Au adsorption. The subsurface O defect V_{sub} is displayed by a dashed circle and the Ce^{3+} ions are shown in dark blue. Both Ce^{3+} are also marked with **1** and **2**. This, relative to the vacant site, symmetric Ce^{3+} configuration having both Ce^{3+} ions in the second cationic coordination shell with respect to V_{sub}, is the most stable Ce^{3+} configuration.[48] Adsorption sites marked by **a** (site near Ce^{3+} and V_{sub}), **b** (near V_{sub}), and **c** (far from Ce^{3+} and V_{sub}) indicate surface oxygen atoms, while **d** indicates the position of a subsurface O (O_{sub}) atom near V_{sub}. The **d** site corresponds to the very stable O_{sub} atop site in the $p(2 \times 2)$ unit cell.

View Article Online
DOI: 10.1039/C7CP01785E

Table 7 Adsorption energies (eV/atom) for one Au atom and the vertical Au_2 dimer on the reduced CeO_{2-x}(111) surface.

DFA	site	*OS(*Au*)*	*p*(2x2)	site	*OS(*Au*)*	*p*(4x4)
PBE+*U*	O-O bridge	+1	-0.69	O-O bridge	+1	-1.15
	O_{surf} atop	0	-0.78[a,b]	O_{surf} atop **a**	0	-0.86
				O_{surf} atop **c**	+1	-0.95
	O_{sub} atop	-1	-0.95	O_{sub} atop **d**	0	-0.76
	Ce^{3+} atop	-1	-0.64	Ce^{3+} atop **1**	δ-	-0.57[c,d]
	Ce^{4+} atop	-1	-0.61			
	V_{surf} atop	-1	-2.44	V_{surf} atop	-1	-2.10
	Au_2 atop V_{surf}	-1[e]	-1.70	Au_2 atop V_{surf}	-1[e]	-1.56[f]
HSE	O_{surf} atop	0	-0.55[a,b]	O_{surf} atop **a**	0	-0.56
				O_{surf} atop **b**	0	-0.60
				O_{surf} atop **c**	0	-0.50
	O_{sub} atop	-1	-0.95	O_{sub} atop **d**	–	–[g]
	Ce^{3+} atop	-1	-0.64	Ce^{3+} atop **1**	–	–[c,d]
	V_{surf} atop	-1	-2.47	V_{surf} atop	-1	-2.16
	Au_2 atop V_{surf}	-1[e]	-1.64			

[a] One imaginary frequency.
[b] Tilting angle of the Au-O bond w.r.t. surface normal ca. 20° (see Table 2).
[c] Upon complete electron transfer [OS(Au) = −1], reconstruction to Au^- atop a surface oxygen vacancy occurs.
[d] Site **1** is symmetry equivalent to site **2**.
[e] Oxidation state of the entire Au_2 dimer (Au_2^-).
[f] Without electron transfer, O_{sub} fills V_{surf} and Au_2 binds at the newly formed O_{surf}. This structure is 0.72 eV lower in energy than Au_2^- atop V_{surf}.
[g] No convergence reached upon several restarts.

Adsorption energies and oxidation states for the $p(2 \times 2)$ and $p(4 \times 4)$ cells obtained with PBE+*U* and HSE are summarized in Table 7. We reproduced the finding reported in ref. 45, hence V_{surf} acts as an effective trap for Au atoms on the reduced CeO_2(111) surface. In atop position of V_{surf}, Au is always negatively charged, i.e. one electron from a Ce^{3+} ion is transferred into the Au 6s orbital. For the $p(2 \times 2)$ cell, HSE predicts slightly more exothermic

View Article Online
DOI: 10.1039/C7CP01785E

binding compared to PBE+*U*. Adsorption at surface oxygen vacancies on the $p(4 \times 4)$ cell is less exothermic, which is explained by (i) the smaller relaxation contribution due to the lower Ce^{3+} concentration (less strain), and (ii) because the electron is transferred from a surface Ce^{3+} ion instead of a subsurface Ce^{3+} ion (see section 3.C). Note that the 2_1-2_2 configuration for the surface defect was not considered in ref. 72. Independent of the approach, it is 0.07 eV more stable than 1_1-2_1, and it has been taken as a reference for Au adsorption in the present work.

Adding a second Au atom, thus building an upright Au_2 dimer at the surface vacancy, is thermodynamically less favourable than the corresponding process on pristine $CeO_2(111)$. This is explained by the occupation of an antibonding orbital of the Au-Au bond upon electron transfer from Ce^{3+}. On the $p(4 \times 4)$ cell, electron transfer is less favourable, and PBE+*U* predicts a reconstruction of this structure to (electro-neutral) Au_2 atop O_{surf}, i.e. an O atom in subsurface position fills V_{surf} (thereby creating V_{sub}).

Results critically depend on the cell size upon adsorbing Au in atop position of O_{sub} (**d** in Fig. 6). For the $p(2 \times 2)$ cell, PBE+*U* predicts an adsorption energy of -0.95 eV involving electron transfer from Ce^{3+} to Au^0, while using the $p(4 \times 4)$ cell yields a significantly lower adsorption energy (-0.74 eV) involving no electron transfer. For the small cell, PBE+*U* agrees with HSE, but for the $p(4 \times 4)$ cell the HSE structure for Au atop **d** turned out to be unstable. Multiple attempts to converge the HSE energy as well as the atomic forces failed. This suggests that the O_{sub} atop site is only relevant at high defect concentrations.

Adsorption of Au atop a Ce^{3+} ion (**1** or **2** in Fig. 6) in the $p(4 \times 4)$ cell using PBE+*U* leads to two different solutions depending on the extent of charge transfer. Upon complete transfer of the Ce 4f electron to the Au, i.e. upon creation of Au^-, reconstruction of the surface occurs. One of the nearest neighbour surface O atoms relaxes into the V_{sub} position, thereby creating V_{surf}, which is filled by Au^-. The driving force for this reconstruction is the very exothermic adsorption energy (-2.10 eV). Upon partial electron transfer, however, Au stays on top of the

View Article Online
DOI: 10.1039/C7CP01785E

Ce ion. Using HSE, partial electron transfer could not be stabilized and hence only the solution involving reconstruction from Au^- atop Ce^{3+} to Au^- atop V_{surf} was found.

Based on HSE results for the $p(4 \times 4)$ unit cell, Au adsorption at the O_{surf} **c** site is 0.10 eV less stable compared with the O_{surf} **b** site, suggesting that adsorption near the vacancy is thermodynamically more favourable. In contrast, PBE+*U* adsorption energies are more exothermic for O_{surf} sites far from the vacancy. A similar trend is found comparing adsorption energies for clean and oxygen-defective ceria. Disregarding Au atop V_{surf}, PBE+*U* adsorption energies are in general more exothermic for the clean $CeO_2(111)$ surface than for the reduced one. In contrast, HSE results for the $p(4 \times 4)$ cell suggest a slightly more exothermic adsorption of Au atoms on the reduced surface.

F. Comparison with other oxides

Adsorption energies of single Au atoms on defect-free metal oxide surfaces and at surface oxygen vacancies are reported in Table 8. As discussed in the previous section, adsorption energies depend on the approach and on the model (e.g., cell size), nonetheless the strong binding of Au to surface oxygen vacancies is obvious. Adsorption at surface O vacancies is accompanied by electron transfer from the support to the adatom except for the SiO_2 bilayer. Similarly, adsorption near subsurface vacancies on anatase $TiO_2(101)$ (-1.61 eV) and $ZrO_2(101)$ (-2.43 eV) is more exothermic compared to respective defect-free surfaces.[79] Most stable structures are Au^- atop Ti^{4+} and Zr^{4+}, respectively. Other electron-rich defects such as Li[80] or Ti[81] dopants in SiO_2/Mo(112) films or additional Ti atoms in rutile $TiO_2(110)$ surfaces[82] also lead to a more exothermic Au adsorption compared to defect-free surfaces.

This work focuses on O vacancies as a source for electrons in the surface, and we refer the interested reader to the large body of work examining metal supported oxide films, where changes in the work function due to the nature of the metal oxide adlayer are crucial for the electron transfer (see ref. 83 and references therein).

View Article Online
DOI: 10.1039/C7CP01785E

Table 8 Au adsorption energies, ΔE_{ads}, in eV and oxidation state of Au, OS(Au), for various supports.

		defect-free surface			surface O vacancy	
support	approach	site	OS(Au)	ΔE_{ads}	ΔE_{ads}	ref.
CeO_2(111)	PBE+*U*(4.5)	O-O bridge	+1	-1.20	-2.44	This
	HSE	O-Ce bridge	0	-0.52	-2.49	work
rutile TiO_2(110)	PW91	O-Ti bridge	δ+	-0.68	-2.33	84
	PBE+*U*(4.2)	O-Ti bridge	δ+	-0.58	-1.54	85
anatase TiO_2(101)	PBE+*U*(3.0)	Ti atop [a]	0	-0.61	-3.07	79
ZrO_2(101)	PBE+*U*(4.0)	O-Zr bridge	0	-1.20	-4.22	79
V_2O_3(0001)	PW91+*U*(2.5)	O-O bridge	δ+	-1.81	-2.04	86
SiO_2 bilayer	PW91	hollow [b]	0	-0.03	-1.18 [c]	81, 87
SiO_2/Mo(112)	PW91	hollow [b]	0	-0.09	-1.80 [d]	81, 87
α-Al_2O_3(0001)	PW91	O atop	0	-0.81		88

[a] Figure 5 in ref. 79 indicates a slight tilting of the Au-Ti bond towards an O atom.
[b] Au adsorbs above the centre of the hexagonal rings.
[c] Au atom remains electro-neutral.
[d] Instead of adsorption at the surface O vacancy, Au may also adsorb at the SiO_2-Mo interface (-2.87 eV).

4. Conclusions

PBE+*U* using U = 4.5 eV applied to Ce 4f predicts Au atoms on the pristine CeO_2(111) surface to preferentially accommodate oxidation state +1, while HSE predicts the oxidation states 0 and +1 to be close in energy. The clear preference of PBE+*U* conflicts with recent experiments, whereas HSE results are reconcilable with observation.[46] Overall, HSE adsorption energies for the pristine surface are significantly less exothermic than corresponding PBE+*U* values.

Regardless of the method employed, surface oxygen vacancies serve as deep traps for single Au atoms. Moreover, we find that the dimerization reaction proceeds less exothermically than the adsorption of a single Au atom at the surface oxygen vacancy.

For the $p(2 \times 2)$ surface unit cell of reduced CeO_2(111), we confirm that Au adsorbed atop of subsurface oxygen in nearest-neighbour position to the surface Ce^{3+} ion represents the most

View Article Online
DOI: 10.1039/C7CP01785E

stable adsorption structure.[73] A qualitatively different picture is obtained for the $p(4 \times 4)$ surface unit cell corresponding to a lower and (with regard to experiment) more realistic defect concentration. In this case, the aforementioned structure is not stable. Instead, PBE+*U* predicts the O-O bridge position to be the most favourable site for Au adsorption, while HSE favours Au atop surface O ions close to the vacancy. Both method as well as O-defect concentration (i.e. size of unit cell) impact stability of donor and acceptor orbitals, in turn affecting relative stabilities of adsorption sites. The DFT+*U* approach is a computationally efficient and useful method; however, for systems involving electron transfer careful checking of results is strongly advised. Although for instance (conventional) hybrid functionals do not properly account for important electron correlation effects like van der Waals dispersion interactions, the complex Au/CeO_{2-x} system appears to be accurately described using hybrids employing ~25% of Fock exchange.

Acknowledgements

It is our pleasure to thank Professor Joachim Sauer and Professor Hans-Joachim Freund for their continuous support and many insightful discussions. We also thank Dr. M. Verónica Ganduglia-Pirovano for some discussions on the topic. This work has been supported by the "Fonds der Chemischen Industrie" (FCI) as well as by grants for computing time at the high-performance computer centers HLRN (North-German Supercomputing Alliance in Berlin and Hannover) and JUROPA (Forschungszentrum Jülich). Furthermore, we acknowledge COST action CM1104 entitled "reducible oxide chemistry, structure, and functions" and the "Stiftung Industrieforschung der Humboldt-Universität zu Berlin" for support.

References

1. M. Haruta and M. Date, *Appl. Catal. A-Gen.*, 2001, **222**, 427-437.
2. M. Haruta, *Cattech*, 2002, **6**, 102-115.

View Article Online
DOI: 10.1039/C7CP01785E

3. M. Haruta, *Chemical record (New York, N.Y.)*, 2003, **3**, 75-87.
4. M. Haruta, *Gold Bulletin*, 2004, **37**, 27-36.
5. A. Trovarelli, *Catalysis by Ceria and Related Materials*, Imperial College Press, London, 2002.
6. Q. Fu, H. Saltsburg and M. Flytzani-Stephanopoulos, *Science*, 2003, **301**, 935-938.
7. Q. Fu, W. L. Deng, H. Saltsburg and M. Flytzani-Stephanopoulos, *Appl. Catal., B*, 2005, **56**, 57-68.
8. G. L. Haller and D. E. Resasco, *Adv. Catal.*, 1989, **36**, 173-235.
9. S. J. Tauster, *Acc. Chem. Res.*, 1987, **20**, 389-394.
10. C. T. Campbell, *Nat. Chem.*, 2012, **4**, 597-598.
11. J. A. Farmer and C. T. Campbell, *Science*, 2010, **329**, 933-936.
12. M. Skoda, M. Cabala, I. Matolinova, K. C. Prince, T. Skala, F. Sutara, K. Veltruska and V. Matolin, *J. Chem. Phys.*, 2009, **130**, 034703.
13. G. N. Vayssilov, Y. Lykhach, A. Migani, T. Staudt, G. P. Petrova, N. Tsud, T. Skala, A. Bruix, F. Illas, K. C. Prince, V. Matolin, K. M. Neyman and J. Libuda, *Nat. Mater.*, 2011, **10**, 310-315.
14. J. L. Lu, H. J. Gao, S. Shaikhutdinov and H. J. Freund, *Surf. Sci.*, 2006, **600**, 5004-5010.
15. J. L. Lu, H. J. Gao, S. Shaikhutdinov and H. J. Freund, *Catal. Lett.*, 2007, **114**, 8-16.
16. C. Zhang, A. Michaelides, D. A. King and S. J. Jenkins, *J. Chem. Phys.*, 2008, **129**, 194708.
17. N. C. Hernandez, R. Grau-Crespo, N. H. de Leeuw and J. F. Sanz, *Phys. Chem. Chem. Phys.*, 2009, **11**, 5246-5252.
18. M. F. Camellone and S. Fabris, *J. Am. Chem. Soc.*, 2009, **131**, 10473-10483.
19. N. V. Skorodumova, R. Ahuja, S. I. Simak, I. A. Abrikosov, B. Johansson and B. I. Lundqvist, *Phys. Rev. B*, 2001, **64**, 115108.
20. G. Kresse, P. Blaha, J. L. F. Da Silva and M. V. Ganduglia-Pirovano, *Phys. Rev. B*, 2005, **72**, 237101.
21. J. L. F. Da Silva, M. V. Ganduglia-Pirovano, J. Sauer, V. Bayer and G. Kresse, *Phys. Rev. B*, 2007, **75**, 045121.
22. V. Ganduglia-Pirovano, A. Hofmann and J. Sauer, *Surf. Sci. Rep.*, 2007, **62**, 219-270.
23. J. Paier, C. Penschke and J. Sauer, *Chem. Rev.*, 2013, **113**, 3949-3985.
24. V. I. Anisimov, J. Zaanen and O. K. Andersen, *Phys. Rev. B*, 1991, **44**, 943-954.
25. A. I. Liechtenstein, V. I. Anisimov and J. Zaanen, *Phys. Rev. B*, 1995, **52**, R5467-R5470.
26. C. W. M. Castleton, J. Kullgren and K. Hermansson, *J. Chem. Phys.*, 2007, **127**, 244704.
27. S. Lutfalla, V. Shapovalov and A. T. Bell, *J. Chem. Theory Comput.*, 2011, **7**, 2218-2223.
28. Z. Hu, B. Li, X. Sun and H. Metiu, *J. Phys. Chem. C*, 2011, **115**, 3065-3074.
29. M. Cococcioni and S. de Gironcoli, *Phys. Rev. B*, 2005, **71**.
30. F. Aryasetiawan, K. Karlsson, O. Jepsen and U. Schönberger, *Phys. Rev. B*, 2006, **74**.
31. A. D. Becke, *J. Chem. Phys.*, 1993, **98**, 5648-5652.
32. J. P. Perdew, M. Ernzerhof and K. Burke, *J. Chem. Phys.*, 1996, **105**, 9982-9985.
33. S. Chawla and G. A. Voth, *J. Chem. Phys.*, 1998, **108**, 4697-4700.
34. J. Paier, R. Hirschl, M. Marsman and G. Kresse, *J. Chem. Phys.*, 2005, **122**, 234102.
35. M. Betzinger, C. Friedrich and S. Bluegel, *Phys. Rev. B*, 2010, **81**, 195117.
36. J. Graciani, A. M. Marquez, J. J. Plata, Y. Ortega, N. C. Hernandez, A. Meyer, C. M. Zicovich-Wilson and J. F. Sanz, *J. Chem. Theory Comput.*, 2011, **7**, 56-65.
37. J. P. Perdew, K. Burke and M. Ernzerhof, *Phys. Rev. Lett.*, 1996, **77**, 3865-3868.
38. S. Fabris, S. de Gironcoli, S. Baroni, G. Vicario and G. Balducci, *Phys. Rev. B*, 2005, **72**, 237102.
39. J. Heyd, G. E. Scuseria and M. Ernzerhof, *J. Chem. Phys.*, 2003, **118**, 8207-8215.
40. J. Paier, *Catal. Lett.*, 2016, **146**, 861-885.
41. Z. P. Liu, S. J. Jenkins and D. A. King, *Phys. Rev. Lett.*, 2005, **94**, 196102.

View Article Online
DOI: 10.1039/C7CP01785E

42. N. J. Castellani, M. A. Branda, K. M. Neyman and F. Illas, *J. Phys. Chem. C*, 2009, **113**, 4948-4954.
43. M. M. Branda, N. J. Castellani, R. Grau-Crespo, N. H. de Leeuw, N. C. Hernandez, J. F. Sanz, K. M. Neyman and F. Illas, *J. Chem. Phys.*, 2009, **131**, 094702.
44. M. M. Branda, N. C. Hernandez, J. F. Sanz and F. Illas, *J. Phys. Chem. C*, 2010, **114**, 1934-1941.
45. C. J. Zhang, A. Michaelides and S. J. Jenkins, *Phys. Chem. Chem. Phys.*, 2011, **13**, 22-33.
46. Y. Pan, Y. Cui, C. Stiehler, N. Nilius and H. J. Freund, *J. Phys. Chem. C*, 2013, **117**, 21879-21885.
47. Y. Chen, P. Hu, M. H. Lee and H. F. Wang, *Surf. Sci.*, 2008, **602**, 1736-1741.
48. Y. Pan, N. Nilius, H.-J. Freund, J. Paier, C. Penschke and J. Sauer, *Phys. Rev. Lett.*, 2013, **111**, 206101, Erratum: ibid. 2015, **115**, 269901.
49. P. Pyykkö, *Angew. Chem., Int. Ed.*, 2004, **43**, 4412-4456.
50. N. A. Deskins, R. Rousseau and M. Dupuis, *J. Phys. Chem. C*, 2010, **114**, 5891-5897.
51. N. A. Deskins and M. Dupuis, *Phys. Rev. B*, 2007, **75**, 195212.
52. J. J. Plata, A. M. Marquez and J. F. Sanz, *J. Phys. Chem. C*, 2013, **117**, 25497-25503.
53. J. J. Plata, A. M. Marquez and J. F. Sanz, *J. Phys. Chem. C*, 2013, **117**, 14502-14509.
54. P. G. Lustemberg, Y. Pan, B. J. Shaw, D. Grinter, C. Pang, G. Thornton, R. Perez, M. V. Ganduglia-Pirovano and N. Nilius, *Phys. Rev. Lett.*, 2016, **116**, 236101.
55. P. E. Blöchl, *Phys. Rev. B*, 1994, **50**, 17953-17979.
56. G. Kresse and D. Joubert, *Phys. Rev. B*, 1999, **59**, 1758-1775.
57. G. Kresse and J. Furthmüller, *Phys. Rev. B*, 1996, **54**, 11169-11186.
58. G. Kresse and J. Furthmüller, *Comp. Mater. Sci.*, 1996, **6**, 15-50.
59. S. L. Dudarev, G. A. Botton, S. Y. Savrasov, C. J. Humphreys and A. P. Sutton, *Phys. Rev. B*, 1998, **57**, 1505-1509.
60. O. Bengone, M. Alouani, P. Blöchl and J. Hugel, *Phys. Rev. B*, 2000, **62**, 16392-16401.
61. A. V. Krukau, O. A. Vydrov, A. F. Izmaylov and G. E. Scuseria, *J. Chem. Phys.*, 2006, **125**, 224106.
62. M. Ernzerhof and G. E. Scuseria, *J. Chem. Phys.*, 1999, **110**, 5029-5036.
63. C. Adamo and V. Barone, *J. Chem. Phys.*, 1999, **110**, 6158-6170.
64. V. N. Staroverov, G. E. Scuseria, J. M. Tao and J. P. Perdew, *J. Chem. Phys.*, 2003, **119**, 12129-12137.
65. J. M. Tao, J. P. Perdew, V. N. Staroverov and G. E. Scuseria, *Phys. Rev. Lett.*, 2003, **91**, 146401.
66. J. Sun, M. Marsman, G. I. Csonka, A. Ruzsinszky, P. Hao, Y.-S. Kim, G. Kresse and J. P. Perdew, *Phys. Rev. B*, 2011, **84**.
67. A. D. Becke, *J. Chem. Phys.*, 1993, **98**, 1372-1377.
68. S. Grimme, *J. Comput. Chem.*, 2006, **27**, 1787-1799.
69. F. D. Murnaghan, *Proc. Natl. Acad. Sci. U. S. A.*, 1944, **30**, 244-247.
70. H. J. Monkhorst and J. D. Pack, *Phys. Rev. B*, 1976, **13**, 5188-5192.
71. G. Makov and M. C. Payne, *Phys. Rev. B*, 1995, **51**, 4014-4022.
72. M. V. Ganduglia-Pirovano, J. L. F. Da Silva and J. Sauer, *Phys. Rev. Lett.*, 2009, **102**, 02610101 - 02610104.
73. K. Kosmider, V. Brazdova, M. V. Ganduglia-Pirovano and R. Perez, *J. Phys. Chem. C*, 2016, **120**, 927-933.
74. J. F. Jerratsch, X. Shao, N. Nilius, H.-J. Freund, C. Popa, M. V. Ganduglia-Pirovano, A. M. Burow and J. Sauer, *Phys. Rev. Lett.*, 2011, **106**, 246801.
75. R. O. Jones and O. Gunnarsson, *Rev. Mod. Phys.*, 1989, **61**, 689-746.
76. F. Fuchs, J. Furthmüller, F. Bechstedt, M. Shishkin and G. Kresse, *Phys. Rev. B*, 2007, **76**, 115109.
77. M. Huang and S. Fabris, *J. Phys. Chem. C*, 2008, **112**, 8643-8648.

View Article Online
DOI: 10.1039/C7CP01785E

78. C. Loschen, J. Carrasco, K. M. Neyman and F. Illas, *Phys. Rev. B*, 2007, **75**, 035115.
79. P. Schlexer, A. R. Puigdollers and G. Pacchioni, *Phys. Chem. Chem. Phys.*, 2015, **17**, 22342-22360.
80. U. Martinez, L. Giordano and G. Pacchioni, *ChemPhysChem*, 2010, **11**, 412-418.
81. L. Giordano, A. Del Vitto and G. Pacchioni, *J. Chem. Phys.*, 2006, **124**, 034701.
82. U. Martinez and B. Hammer, *J. Chem. Phys.*, 2011, **134**, 194703.
83. G. Pacchioni and H.-J. Freund, *Chem. Rev.*, 2013, **113**, 4035-4072.
84. A. Vijay, G. Mills and H. Metiu, *J. Chem. Phys.*, 2003, **118**, 6536-6551.
85. M. F. Camellone, P. M. Kowalski and D. Marx, *Phys. Rev. B*, 2011, **84**, 035413.
86. N. Nilius, V. Brazdova, M. V. Ganduglia-Pirovano, V. Simic-Milosevic, J. Sauer and H. F. Freund, *New J. Phys.*, 2009, **11**, 093007.
87. U. Martinez, L. Giordano and G. Pacchioni, *J. Phys. Chem. B*, 2006, **110**, 17015-17023.
88. N. C. Hernandez, J. Graciani, A. Marquez and J. F. Sanz, *Surf. Sci.*, 2005, **575**, 189-196.

View Article Online
DOI: 10.1039/C7CP01785E

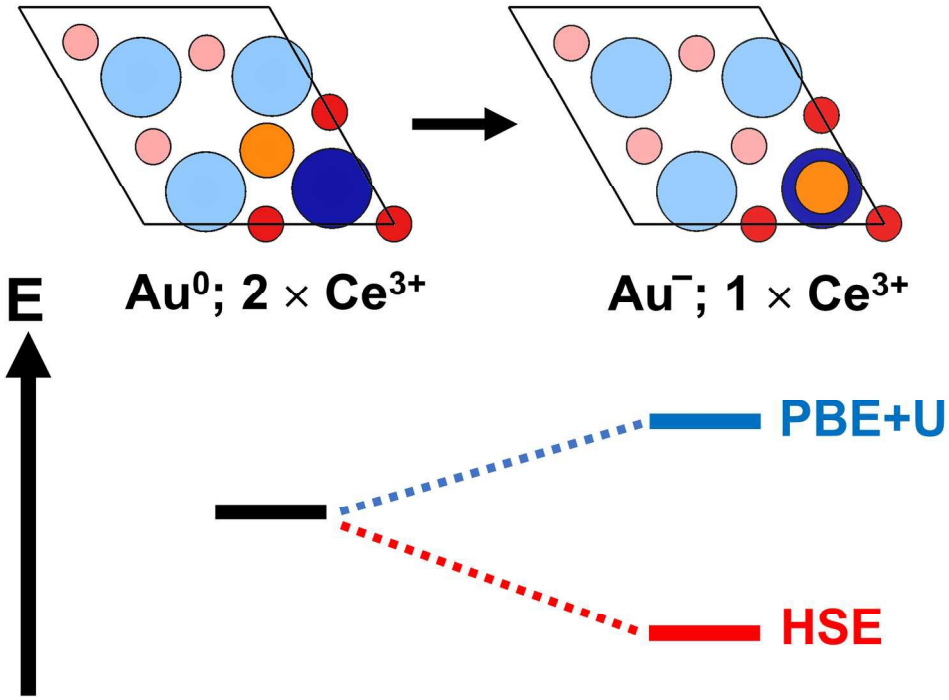

190x142mm (300 x 300 DPI)